Journal of the European Ceramic Society 40 (2020) 1791–1800

Contents lists available at ScienceDirect

Journal of the European Ceramic Society

journal homepage: www.elsevier.com/locate/jeurceramsoc

Original Article

The irradiation response of ZrC ceramics under 10 MeV Au^{3+} ion irradiation at 800 ºC

Raul Florez[a], Miguel L. Crespillo[b], Xiaoqing He[c,d], Tommi A. White[c,e], Gregory Hilmas[f], William Fahrenholtz[f], Joseph Graham[a,f,*]

[a] Nuclear Engineering Program, Missouri University of Science and Technology, 65409 Rolla, MO, United States
[b] Department of Material Science and Engineering, University of Tennessee, 37996 Knoxville, TN, United States
[c] Electron Microscopy Core, University of Missouri, 65211 Columbia, MO, United States
[d] Department of Mechanical and Aerospace Engineering, University of Missouri, 65211 Columbia, MO, United States
[e] Department of Biochemistry, University of Missouri, Columbia, MO, 65211, United States
[f] Department of Materials Science and Engineering, Missouri University of Science and Technology, 65409 Rolla, MO, United States

ARTICLE INFO

Keywords:
Ion irradiation
ZrCx
XRD
TEM
Raman

ABSTRACT

The microstructural evolution was characterized for ZrC ceramics irradiated with 10 MeV Au^{3+} ions at 800 °C. Post-irradiation examination showed that ZrC did not amorphize at doses up to 30 displacement per atoms (dpa). Concurrent oxidation of ZrC was found to occur during ion irradiation. Coarsening of the defective microstructure, as a function of dose, was revealed by transmission electron microscopy analysis. Black dot defects were observed at low doses (0.5 dpa), and tangled dislocation networks were formed at 5 dpa and above. Diffraction analysis showed a change in the defect structure occurred at doses close to ~2.5 dpa. The evolution of lattice parameter with dose indicated that uptake of adventitious oxygen could occur in specimens irradiated at high doses. Raman spectroscopy analysis indicated an increase in non-stochiometry after irradiaton. This work identified specific relationships between dose and microstructure after irradiation, revealing the mechanisms of damage production in ZrC_x ceramics.

1. Introduction

Zirconium Carbide (ZrC_x) is a ceramic material that exhibits high melting temperature and Vickers hardness [1], excellent high-temperature thermal and mechanical properties [2], adequate corrosion resistance to fission products [3,4], and low neutron absorption cross section [1,5]. This unusual combination of properties makes ZrC an attractive candidate for a variety of elevated-temperature nuclear applications, including fuel cladding and inert fuel matrix materials for Gen-IV gas-cooled reactors [6,7], structural components in fusion reactors [8], and as a coating in Trisostructural-Isotropic (TRISO) fuel particles [9–11]. In these applications, ZrC_x would be exposed to neutron and ion irradiations [12,13]. As a result, atomic defects, lattice disorder, and other radiation-induced microstructural modifications are expected to occur due the substantial amount of energy deposited in the target material under irradiation. The formation and distribution of radiation-induced defects can significantly affect the mechanical, thermophysical, and chemical properties of ZrC_x after irradiation [14–16]. Consequently, successful implementation of ZrC_x in nuclear systems requires investigation of its radiation response mechanisms and the concomitant radiation effects on the properties.

During the last three decades, a great number of experimental [17–21] and theoretical investigations [22–25] have been dedicated to understanding the fundamental processes that govern the radiation response of ZrC_x. The majority of studies to date have focused on characterizing the radiation damage produced by nuclear elastic interactions (*i.e.* ballistic damage), which is most relevant to the operational performance of ZrC_x subject to neutron fluxes in nuclear reactors [26]. To this end, intermediate-energy heavy ions and protons from ion accelerator facilities have been widely used to emulate ballistic damage under well-controlled irradiation conditions and high displacement doses [27]. Ballistic collisions displace atoms from their equilibrium positions, initiating a series of structural changes within the target material, which are dependent on the rate of production, annihilation, and agglomeration of the radiation-induced point defects at a given temperature [28]. Using this approach, systematic studies have been conducted for ion irradiation of ZrC_x at multiple irradiation conditions over the temperature range of 20 − 1073 K [29–31]. The ion irradiated

* Corresponding author at: Nuclear Engineering Program, Missouri University of Science and Technology, 65409 Rolla, MO, United States.
E-mail address: grahamjose@mst.edu (J. Graham).

https://doi.org/10.1016/j.jeurceramsoc.2020.01.025
Received 13 August 2019; Received in revised form 10 January 2020; Accepted 13 January 2020
Available online 14 January 2020
0955-2219/

microstructures have been characterized with a number of techniques including transmission electron microscopy (TEM), X-ray diffraction (XRD), ion channeling Rutherford backscattering spectrometry (RBS/c), and Raman spectroscopy. No amorphization has been observed in any of the above studies, demostrating the superior structural stability and radiation tolerance of ZrC_x over the temperature range investigated.

Previous studies suggested that within the operational temperature range of high temperature nuclear reactors (600 − 1100 °C), the radiation response of ZrC_x is driven by interstitial clustering [32]. Due to the high melting point of ZrC (T_m = 3420 °C [33]), vacancy mobility is not expected when $T_{irr} < 0.3T_m$. In contrast, interstial atoms are highly mobile even at RT and immediately tend to cluster to form dislocation loops under far from equilibrium conditions [25]. These observations have been validated experimentally by TEM anlaysis, through which "black dot" defects and dislocation loops have been observed as the primary type of defects in irradiated ZrC_x [12,29–31]. The clustering of interstitials in irradiated ZrC_x has also been reproduced numerically using DFT-informed Cluster Dynamic simulations [32]. In the low homologous temperature regime, where interstials are mobile and vacancies are sessile, two competing process occur simultaneously: dislocation loop nucleation and interstitial capture by dislocation loops. Initially at lower doses (~ < 1 dpa), the rate of nucleation of interstitial clusters outpaces the rate of loop growth because the density of dislocation loops is low. When increasing the irradiation dose, new interstital clusters are more likely to coalesce with each other to form dislocation loops. These loops will continue to grow in size and density until a critical dose is reached. At this point, the rate of dislocation loop nucleation is reduced because the defect clusters generated by irradiation are more likely to coalesce with the already nucleated dislocation loops. Consequently, irradiation beyond this threshold dose will produce coarsening of dislocation loops that are already formed. As dislocation loops grow, each will become an increasingly larger sink for defects, so the nucleation rate of loops should continue to drop until saturation is reached. As a result, a saturation in the density of dislocations is also expected with the increase in the irradiation dose.

Although a coarse understanding of the radiation response of ZrC_x can be drawn from the existing literature, more studies are needed to complement the previously reported experimental data and provide a comprehensive understanding of the performance of ZrC_x within the typical temperature (600 − 1100 °C) and dose range (0.5–50 dpa) of high temperature nuclear reactors (HTRs) [34]. In this regard, only a limited number of studies have been conducted on high-temperature ion irradiation of ZrC at high doses. Moreover, knowledge of the radiation response of ZrC_x ceramics at different length scales is still scarce. This information is particularly relevant for future fission Gen-IV reactors and fusion reactors which require materials to reliably operate at higher temperatures and/or radiation damage levels than those of existing commercial power reactors [35].

The purpose of the present study was to investigate the microstructural evolution of heavy ion irradiated ZrC_x at dose and temperature conditions relevant to the operation of high temperature nuclear reactors.

2. Experimental procedure and methods

2.1. Sample preparation

ZrC billets were prepared by the hot pressing commercial ZrC powder (Alfa Aesar, Reactor Grade, USA), which had a reported purity of 99.5 wt.%, (impurities (wt.%): Al 0.01, Hf < 0.003, Ti 0.009, Cd 0.0002, Cr 0.0003, Mg 0.0006, Pb 0.002). The billets were hot pressed in a graphite die (diameter = 25 mm) using cylindrical graphite spacers (thickness = 10 mm). The inner walls of the die and the faces of the spacers were lined with a BN-sprayed graphitized foil to prevent a reaction between the powder compact and the graphite die. ZrC powder was loaded into the die and cold-compacted using a uniaxial press with an applied pressure of 4 MPa. The die was then placed into a resistively-heated graphite hot press (Model HP20-3060, Thermal Technology Inc., Santa Rosa, CA). Once loaded into the hot press, the chamber was evacuated and backfilled with argon three times. Billets were hot-pressed at 2200 °C and 32 MPa for 2 h to promote full densification. A heating rate of 20 °C/min was used.

The density of the hot-pressed billets was measured by Archimedes' method using distilled water as the immersing medium, according to ASTM C733 [36]. The relative density was calculated by dividing the Archimedes' density by the estimated theoretical density of ZrC (ρ_T = 6.646 g/cm^3). The theoretical density was determined using the experimental carbon content and lattice parameter of as-sintered $ZrC_{0.99}$. The chemical analysis for carbon, oxygen and nitrogen contents of the billet was conducted by the direct combustion method using the infrared absorption detection technique. Carbon (CS600; Leco, St. Joseph, MI), oxygen and nitrogen (TC500; Leco, St. Joseph, MI) contents were measured by crushing dense specimens to ~200 mesh. Three measurements were conducted for each element to establish repeatability.

Following densification, specimens for microscopy and ion irradiations were cut parallel to the hot pressing direction of the billet with a slow-speed diamond saw and then ground and polished to mirror-finish. The metallographic preparation was carried out by grinding the specimens with 100, 320, 600, and 1200 grit SiC pads and water lubricant. Felt pads and water-based diamond slurry suspensions were used for abrasive sizes from 3 µm to 0.025 µm. After polishing, the specimens were ultrasonically cleaned with ethanol for 15 min at room temperature.

2.2. Ion irradiation

A rectangular ZrC polished section (13 × 8 mm) was irradiated in the Ion Beam Materials Laboratory (IBML UT-ORNL) at the University of Tennessee, Knoxville [37] with 10 MeV Au^{3+} ions at 800 °C using a 3.0 MV tandem accelerator. Five different regions of the ZrC specimen (3 × 3 mm each) were irradiated to doses of 0.5, 2.5, 5, 10 and 15 dpa. The total sample area was thus comprised of the five non-overlapping irradiated regions and one unirradiated control region. An additional ZrC polished section was also irradiated to a dose of 30 dpa at the same temperature. Adjustable beam slits were used to define the irradiation areas. The ion beam was defocused and rastered in the horizontal and vertical directions with the aim of producing a region that was homogeneously irradiated. Beam homogeneity was verified by ion-induced luminescence from quartz targets and was found to be within 10% throughout the irradiated area [38]. The flux was set at 1.0×10^{12} cm^{-2} s^{-1} for all fluences. Low beam current densities in the range of 5 nA mm^{-2} were used to reduce any undesired effect and charge accumulation on the samples [39]. The vacuum chamber pressure was observed to be below 6.7×10^{-6} Pa prior to the sample heating process. During sample heating, the chamber pressure initially rose before decreasing to a range of 4–6.7×10^{-5} Pa during irradiation. The maximum outgassing of the specimen was observed around 170 °C with vacuum pressure levels of 1.04×10^{-3} Pa. The Stopping and Range of Ions in Matter binary collision approximation (BCA) code 2013 version (SRIM-2013) [40] was used to estimate the displacement damage depth profile. Cascades were performed in quick-cascade mode (simple Kinchin and Pease model), assuming a target density of 6.646 g/cm^3 and threshold displacement energies of 37 eV for Zr and 16 eV for C. To compare ion and neutron irradiation results, the use of the quick Kinchin–Pease option in SRIM to compute radiation damage exposure has been recommended [41] within the nuclear community and has been widely used in previous studies of ion-irradiated ZrC [17,18,32]. The damage profile estimated from SRIM is determined by the sum of the predicted vacancy concentrations (using 'Knock-Ons' from Au ions and 'Vacancies' from target elements of Zr and C), together with the replacement collisions [42]. Assuming a bulk ZrC sample, the

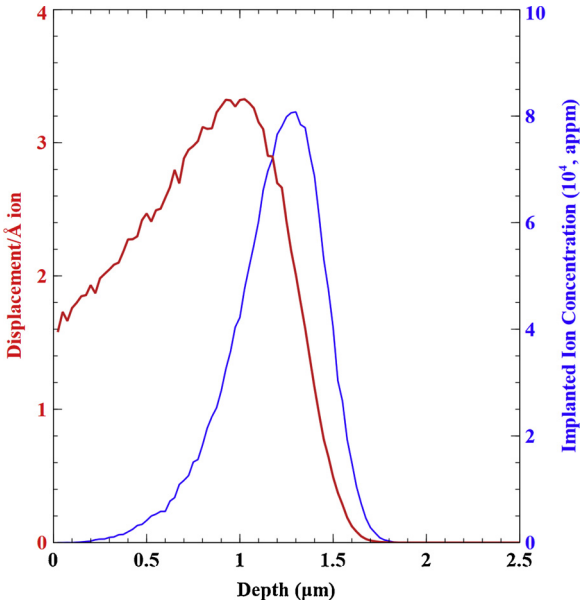

Fig. 1. Depth profile of damage level using SRIM Kinchin and Pease calculations, and Au concentration as a function of depth for a fluence of $3.59 \times 10^{15}\,cm^{-2}$.

predicted damage profile in displacements per atom (dpa), and the implanted Au ion profile, are shown in Fig. 1. The peak dose under 10 MeV Au irradiation is located around 1000 nm. The conversion factor from ion fluence ($10^{14}\,cm^{-2}$) to local dose in the ZrC foil under quick simulation was 0.8343 dpa. The steady state temperature of the sample surface was measured via a K-type (chromel-alumel) thermocouple (TC). The TC was attached to the sample surface by molybdenum spring-loaded clips. Samples mounted on the high temperature stage were conductively heated from the platen. The rear of the platen was radiatively heated using a resistively heated tungsten filament (ERH series heater and EPS-500 power supply, Thermionics Northwest, Inc.). High performance silver paste was used to improve the thermal contact between the bottom surface of the sample and the platen. More details on the experimental apparatus are provided elsewhere [37,39]. Irradiations were performed with Au ions because of their relatively inert nature and large nuclear stopping cross section, which produces a high damage rate per incident ion and minimizes artifacts induced by the injected ions. It is worth noting that a 10 MeV energy beam was chosen to obtain a relatively flat profile to a depth of 1 μm without appreciable effects of implanted Au ions (Fig. 1). Moreover, intermediate energy heavy ion irradiations produce a displacement cascade density and morphology more similar to fission neutrons than light ion irradiation, which produce a more space sub-scale morphology [27]. The temperature and range of doses were selected with the goal of studying radiation damage mechanisms and their effects on microstructural evolution and physical property changes in Gen-IV high temperature gas cooled reactors [35].

2.3. Material characterization

2.3.1. Grazing incidence X-Ray diffraction (GIXRD)

Grazing incidence X-ray diffraction measurements were performed to evaluate structural modifications in the near surface region following high temperature ion irradiations. GIXRD profiles were collected on a PANanlytical X'Pert Pro Multipurpose Diffractometer (MPD) fitted with a Cu X-ray tube and an X'Celerator detector. Diffraction patterns were acquired in grazing incidence geometry over the 2θ range 25-90° with a step size of 0.03° and counting time of 0.5 s at each step. The scans were recorded at several incident angles between 0.5 and 5° in order to probe microstructural changes at different depths from 0.6 to 1.5 μm (Fig. 2).

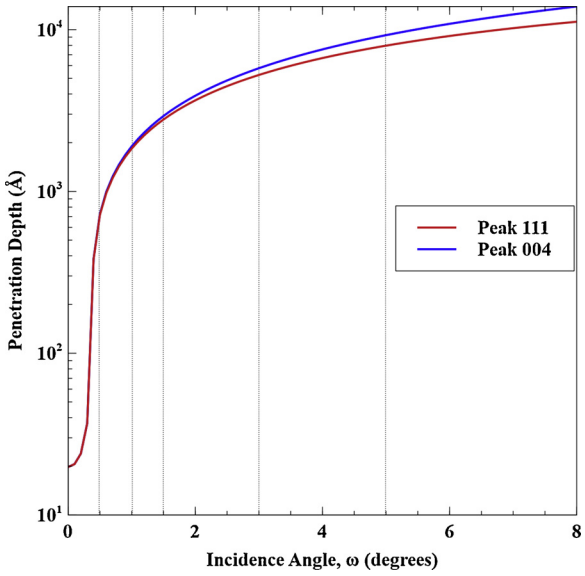

Fig. 2. The scattering depth, Λ, from which diffraction data was collected as a function of the x-ray incident angle for two diffraction peaks, (111) and (400). The x-ray incident angles used in this work are denoted by vertical dashed lines.

X-ray tube operation conditions were 40 kV and 40 mA. The lattice parameter was refined by Rietveld analysis in the full matching pattern mode with the Fullprof suite software [43].

2.3.1.1. Line profile analysis. The values for the size of coherent diffracting domains and microstrains were determined using Williamson-Hall analysis. Peaks obtained from only Cu $k_{\alpha 1}$ radiation were analyzed after stripping Cu $k_{\alpha 2}$ peaks using the classical Rachinger's method [44]. Instrumental broadening was described using a Caglioti polynomial expression obtained by line profile fitting of LaB_6 standard powder (SRM 660a) over the 2θ range investigated. The instrumental integral broadening, thus defined, was subsequently subtracted from the measured integral breadth of the samples to obtain the structural line broadening β.

The coherent diffracting domain sizes (D_v) and microstrains (ε) were obtained from the ordinate intercepts and the slopes, respectively, of straight lines in the Williamson–Hall plots, according to the following equation:

$$\beta\cos(\theta) = \frac{\lambda}{D_v} + 4\varepsilon\sin(\theta) \quad (1)$$

where β is structural line broadening of the reflection, 2θ is the peak position angle, and λ is the monochromatic x-ray wavelength.

2.3.2. Electron microscopy

Surface morphology and composition were examined for both pristine and irradiated materials by focused ion beam (FIB)-scanning electron microscopy (FIB SEM, Scios™ DualBeam™, FEI, Hillsboro, Oregon) coupled with energy dispersive spectroscopy (EDS; Oxford Instrument Avignon UK). TEM specimens were also prepared using the focused-ion-beam (FIB) lift-out technique. Before milling, a 2 μm thick Pt layer was deposited on the top surface of the specimen to protect it from ion beam-induced damage and unwanted surface milling during the FIB preparation. The trenching on both sides was performed at an ion beam voltage of 30 kV with a beam current of a few nanoamps. After lift-out, thinning of the lamella was first conducted with a beam current of hundreds of picoamps at 30 kV at ± 5° on both sides using cleaning cross-section mode until the lamella was ~1 μm thick. Voltages and currents were gradually reduced, and the milling angles decreased, as the lamella got thinner. To complete the preparation, gentle polishing with Ga^+ ions (5 keV and 48 pA) at ± 7° in regular

rectangular mode was used to reduce damage and artifacts of ion implantation caused by higher energy Ga bombardment. Microstructure characterization was performed using a 300 kV Tecnai F30 Supertwin transmission electron microscope (TEM). Bright field (BF) images were acquired under a $g = 220$ two beam condition with the deviation vector $\boldsymbol{s}$ being slightly positive.

2.3.3. Raman spectroscopy

Raman measurements were collected using a HORIBA Jobin Yvon LabRAM ARAMIS microRaman spectrometer (Horiba, Edison, NJ). The specimens were excited by a 632 nm He/Ne laser focused to a spot 2 − 3 μm in size on the sample using a 50x microscope objective lens. Raman spectra were acquired in the backscattering geometry. The laser power was below 2 mW to prevent local heating of the sample. Five spectra were taken from each specimen, with all measurements conducted at room temperature.

3. Results and discussion

3.1. Control specimen

Gas fusion analyses indicated that as-sintered ZrC_x contained 11.62 wt.% carbon, 0.144 wt.% oxygen, and 0.0251 wt. % nitrogen. Consequently, the carbon content of the fabricated billet corresponded to a carbon stoichiometry of $ZrC_{0.99}$. The uncertainty of the gas fusion analyses is estimated at ± 2 wt.%, corresponding to an uncertainty in the stoichiometry of ZrC_x of about ± 0.02.

The bulk density of the as-sintered specimen measured by Archimedes' method was 6.447 g/cm^3, corresponding to a relative density of approximately 97%. Additionally, SEM images of the polished cross section of the billet showed a homogeneous microstructure of ZrC grains with some residual closed porosity. The average grain size measured by the lineal intercept length method was 5.1 ± 1.8 μm. This value agrees with the reported grain size for ZrC ceramics prepared under similar sintering conditions, ranging from to 2 to 30 μm [45,46].

Fig. 3a shows survey GIXRD patterns, obtained at ω values of 0.5, 1, 1.5, 3 and 5°, from the unirradiated ZrC sample after annealing for 5 h at 800 °C in the ion beam line vacuum chamber. The XRD profiles show the expected FFC peaks for ZrC from the (111), (002), (022), (113), (222), and (004) planes corresponding to 2θ values of 32.98, 38.27, 55.26, 65.90, 69.23, and 82.03°, respectively. In addition, the patterns exhibited a low intensity peak at 2θ = 30.11°, that was attributed to the presence of ZrO_2. This peak could not be indexed unequivocally because the monoclinic, tetragonal and cubic forms of ZrO_2 all have peaks close to 2θ = 30°; making them undistiguahable from each other using just this single peak. While it is possible, in principle, to identify the monoclinic phase of ZrO_2 using the weaker peaks at ~18° and ~25°, the maximum intensity of those peaks was below the detection limit in the scans. Therefore, the absence of those peaks was no taken as conclusive evidence for the absence of the monoclinic phase. Thus, the unirradiated ZrC specimens appear to contain some ZrO_2 in the near surface region, after annealing, that was not detected in the as-processed materials.

Fig. 3b shows a magnified view of the most intense (111) ZrC diffraction peak. Increasing the incident angle (i.e., increasing the x-ray penetration depth into the specimen) led to increased peak intensity and a reduction of the peak breadth. Similar behavior was also observed for the other ZrC peaks. Concurrent reduction in peak breadth and increased peak intensity with increasing incident angle are indicative of hererogeneous microstrain near the surface [47]. The average microstrain values as a function of the incident angle were determined using Williamson-Hall analysis (Fig. 4a). The unirradiated sample exhibited a microstrain of $\varepsilon = 0.26 \pm 0.02\%$ at the lowest incidence angle ($\omega = 0.5°$). The microstrain decreased at a larger penetration depth probed using ω = 1, 1.5, 3 and 5°, suggesting that the region of highest strain is localized within the first 20 nm of depth from the top surface. The main sources of microstrain could be the difference in the molar volume and thermal expansion coefficient between the major phase, ZrC, and the minor phase of ZrO_2 that was detected; although some residual microstrain could have been introduced during polishing steps used to prepare the surfaces that were irradiated.

The formation of the oxide phase near the surface of the annealed ZrC was confirmed by SEM observations (Fig. 5). Annealing produced discrete nanosized nodules distributed across the surface of annealed specimen that were not present in the original polished surface. The nanoprecipitates ranged in sizes between 20 and 100 nm. Energy dispersive spectroscopy (EDS) analysis indicated that Zr, C and O were the major constituents on the top surface area of the annealed sample. This suggests that the nanoprecipitate nodules observed in the SEM images correspond to the nuclei of the oxide phase detected by GIXRD measurements. Some precipitate-free zones were observed near the grain boundaries of the substrate, which were also revealed due to thermal

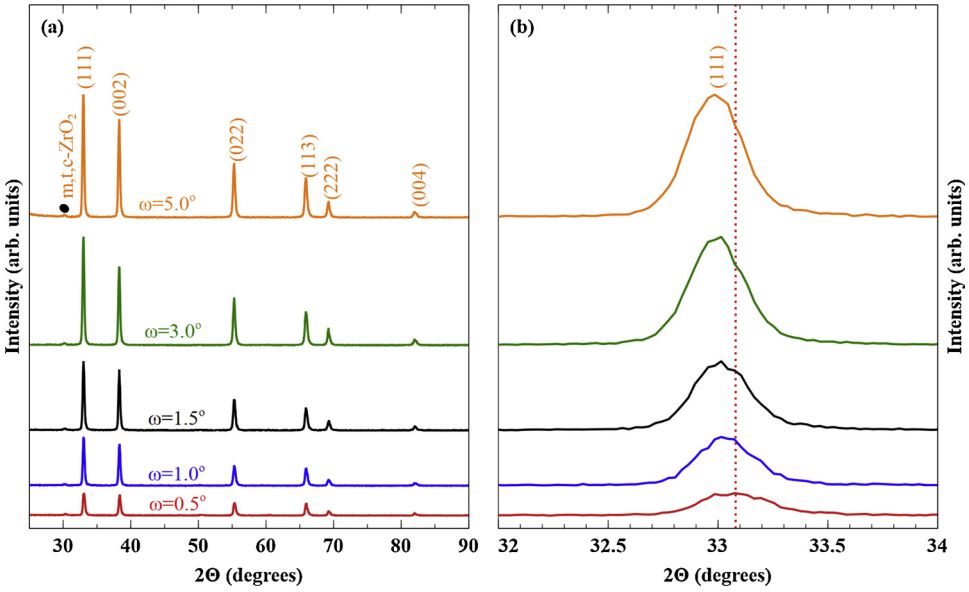

Fig. 3. (a) GIXRD obtained from ZrC after thermal annealing in the ion irradiation chamber at 800 °C, collected at various x-ray incident angles. (b) An enlarged view of the most intense (111) ZrC diffraction maxima.

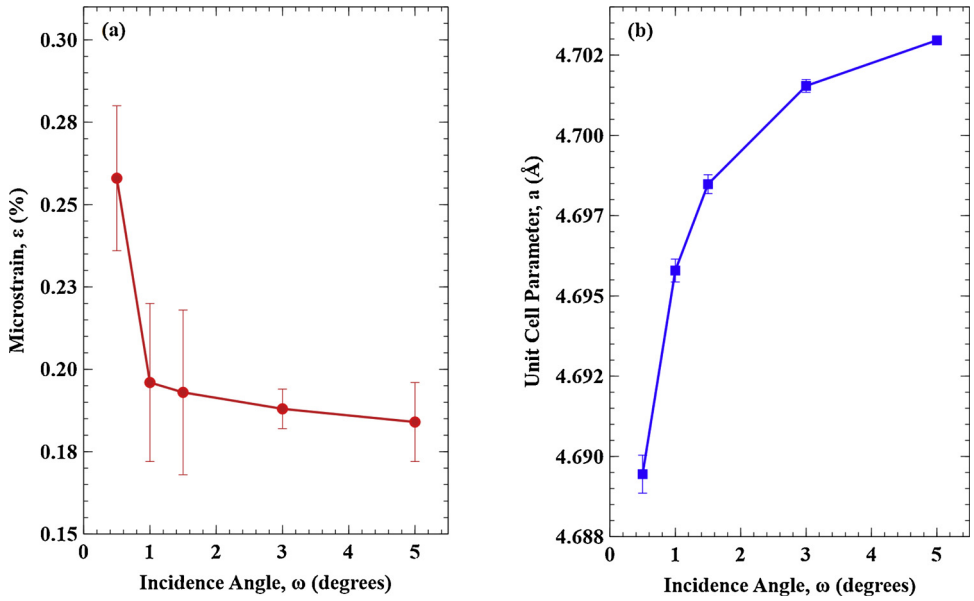

Fig. 4. (a) Heterogeneous microstrain of control sample determined using Williamson–Hall plots as a function of the X-ray incident angle. (b) Unit cell parameter of ZrC for the control specimen as a function X-ray incident angle.

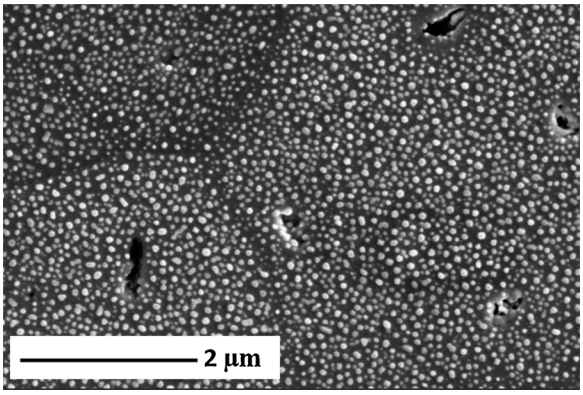

Fig. 5. A secondary electron SEM image of the surface topography showing ZrO_2 nanometric nodules.

etching during annealing.

Further analysis of the (111) ZrC reflection (Fig. 3b) revealed that the location of the diffraction maxima shifted to higher 2θ angles as ω decreased. This suggests that the lattice parameter of ZrC was lower near the surface (Fig. 4b), which could arise from dissolution of adventitious oxygen into the ZrC lattice during annealing. Oxygen uptake result, which is sometimes described as the formation of an oxycarbide (ZrC_xO_y) compound, does not change the structure of ZrC, but decreases the lattice parameter [48]. The contraction of the unit cell results from the strengthening of the metal-non-metal bonds upon incorporation of oxygen into vacant sites in the unit cell [49]. This agrees with the previous work by Gendre, who showed the lattice size of ZrC decreased with oxygen content up to a stoichiometry of around $ZrC_{0.79}O_{0.13}$ [50].

3.2. Irradiated specimens

3.2.1. GIXRD and TEM analysis

Fig. 6a shows representative GIXRD patterns of ZrC samples after irradiation with 10 MeV Au^{3+} at 800 °C. The diffraction patterns were acquired at ω = 1.5° to probe a suitable artifact-free midrange region of the implantation profile (see Fig. 2). Similar to the control specimen, the main peaks indexed to ZrC, and low intensity ZrO_2 peaks were observed at 2θ = 30.11° for the irradiated specimens. Upon irradiation, three major changes were observed in the XRD patterns: shifts of the diffraction maxima, peak broadening, and reduction in the intensities. No evidence of amorphization was observed in any of the samples irradiated at 800 °C, confirming the outstanding stability of ZrC under irradiation. Similar results have been previously reported in neutron and ion irradiation experiments of ZrC at both room temperature and high temperature [29–31]. The most obvious effects of increasing the irradiation dose are a decrease in ZrC peak intensity and an increase in peak broadening. These changes occur due to the microstructural distortions and heterogeneous microstrain associated with the formation of radiation-induced defects. In this regard, the defects present in the irradiated materials distort the long range symmetry of the ideal rock-salt crystal structure, resulting in a partial loss of the coherent scattering and the concomitant decrease in peak intensity. On the other hand, the increased peak broadening can also be ascribed to the accumulation of heterogeneous microstrain and/or the reduction of the coherent scattering domain size.

Williamson-Hall analysis was applied to irradiated samples. W-H plots for the irradited samples are shown in Fig. 7(a). With the exception of the specimen irradiated to 2.5 dpa (Fig. 7b), no anisotropic peak broadening was observed along any specific crystallographic direction in the diffraction pattern of the irradiated samples. The strong peak broadening anisotropy at 2.5 dpa was accompanied by an increased diffuse scattering and a significant reduction of the peak intensity. These concurrent changes are indicative of an increased atomic disorder, which could be due to point defects and dislocation loops. The scattering of X rays from point defects and clusters contribute to diffuse scattering very close to the Bragg peak, which is known as Huang scattering [51]. This type of scattering can be evaluated to analyze the defects in the irradiated sample; however, the GIXRD measurements in this study were conducted at room temperature and the Huang scattering near the Bragg region is superimposed by thermal diffusion scattering, making its evaluation difficult. Since the W-H analysis for the sample irradiated to 2.5 dpa was confounded by these other effects, this specimen was not considered in the subsequent line-broadening analysis. The W-H plots indicated that grain size did not change significantly, but strain increased with increasing dose. This indicates that the XRD peak broadening is primarily due to strain, rather than a reduction in grain size. The average microstrain values for the irradiated samples obtained are shown in Fig. 8(a). It is noted that the average microstrain increased with the irradiation dose and then saturated at

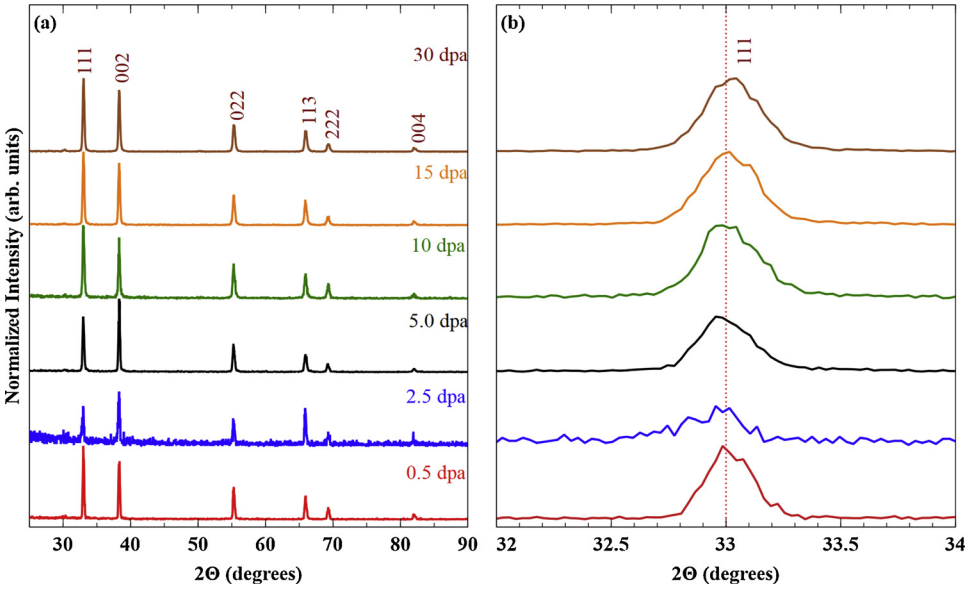

Fig. 6. GIXRD patterns of ZrC after irradiation with 10 MeV Au^{3+} ions to different doses showing (a) the entire pattern and (b) an enlarged view of the (111) diffraction peak.

doses above 5 dpa with $\varepsilon_{sat} \sim 2.2 \times 10^{-3}$.

Saturation of the dislocation density at high doses could explain the microstrain trend observed in this work. At low doses (0.5 dpa), the radiation-induced interstitial clusters have sizes in the order of a few nanometer (< 5 nm) and their density is low. Therefore, the microstrain value observed at 0.5 dpa is also low ($\sim 1.2 \times 10^{-3}$). Fig. 9a shows an on-zone axis bright field TEM micrograph of the sample irradiated at 0.5 dpa. The image reveals the presence of "black dot" defects, which are likely to be small interstitial clusters formed by the ion irradiation. No dislocation loops, with or without double arc-contrast, are observed in the micrograph. Similar results have been obtained in previous TEM work of ion irradiated ZrC at low doses and high temperatures [29,30]. On the other hand, at doses higher than 5 dpa, it can be hypothesized that ZrC has already reached the saturation point in the coarsening-dominant regime. In other words, the rate of dislocation loop nucleation has dropped to a steady state value, and therefore the radiation-induced dislocation structure does not undergo further coarsening. This hypothesis is consistent with the previous in-situ TEM study by Ulmer et al. [30], which noted that the microstructure of ZrC, irradiated with 1 MeV Kr ions at 800 °C, continued to coarsen until doses of 5.1–7.7 dpa. Beyond this dose, a tangled dislocation network formed, and little change was observed in the irradiated microstructure. In this work, "cellular-like" dislocation networks were also observed in bright-field (BF) images of the irradiated microstructure at doses above 5 dpa (Fig. 9b and c). This suggests that at high doses (> 5 dpa), a balance was reached between irradiated-induced damage buildup and dynamic annealing of defects at 800 °C.

Fig. 8b shows the evolution of the ZrC lattice parameter as a function of the dose obtained by refinement of the peak shifts in the XRD patterns. Interestingly, the evolution of the unit cell parameter in this study is not consistent with a single impact mechanism for damage accumulation. This result differs from previous observations by Gosset et al. [52], who reported a saturation of the cell parameter evolution for ZrC irradiated with 4 MeV Au ions at room temperature. In the present study, the unit cell parameter of ZrC exhibited a complex, non-monotonic behavior as a function of dose. Initially, the unit cell parameter increased until reaching a dose of 2.5 dpa. Then, above this critical dose, the lattice parameter decreased. The recovery of the unit cell

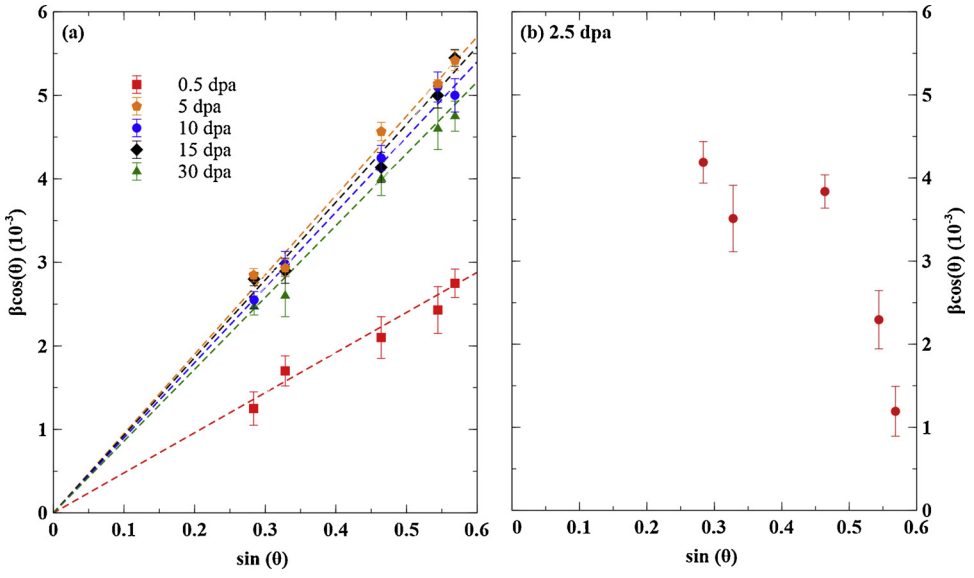

Fig. 7. (a) Williamson-Hall plots of the representative XRD data from irradiated ZrC. Straight lines correspond to the linear fit to the peaks for each dose. The slopes are proportional to the amount of heterogeneous strain present, while their y-intercepts are inversely proportional to the average grain size, (b) Williamson-Hall plot of the specimen irradiated to 2.5 dpa.

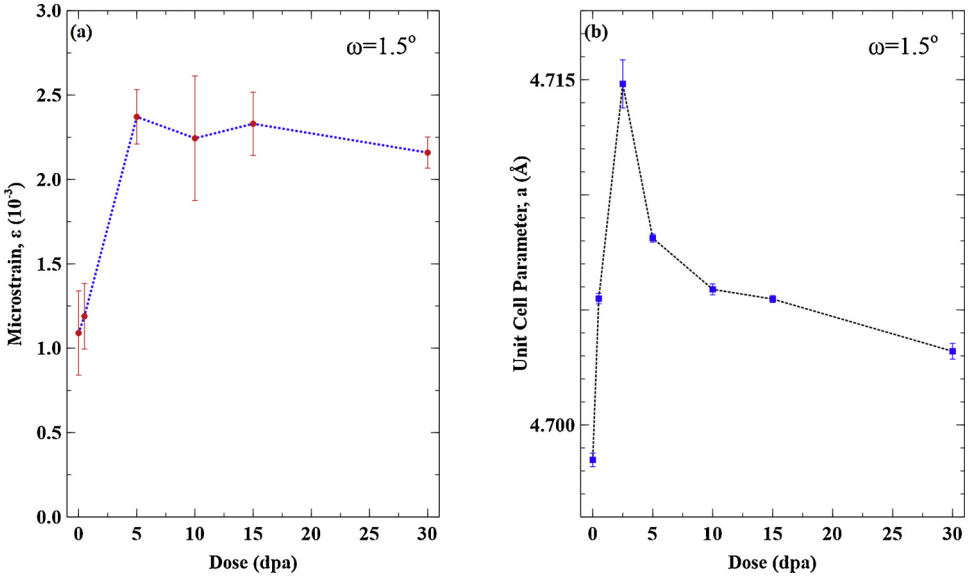

Fig. 8. (a) Heterogeneous microstrain determined using Williamson–Hall plots as a function of dose, (b) Changes in the unit cell parameter of ZrC as a function of dose based on the refinement of the corresponding XRD patterns.

parameter is consistent with a two-step damage accumulation process, which has been previously observed in single crystal ZrC and other non-amorphizable ceramics under irradiation in the nuclear energy loss regime [53,54]. According to this mechanism, a build-up of elastic strain is observed at the early stages of the damage process due to the production and clustering of Frenkel Pair (FP) defects. The accumulation of FPs leads rapidly to the formation of dislocation loops that continue to grow in size as the dose level is increased. Eventually, at the threshold dose, the dislocation loops come into contact with each other and form an entangled dislocation network. This transformation in the defect structure is accompanied by an elastic strain relaxation due to the plastic deformation associated with the production of extended defects. According to Pellegrino et al [32], the critical fluence for this transition is about 5×10^{18} ions/m^2 ($\sim$2.2 dpa) for Au ions in ZrC. This value is close to the transition dose for unit cell parameter recovery that is observed in this work. However, another explanation will be required to account for the reduction of the unit lattice parameter at higher doses, where the structure of the dislocation network is no longer coarsening.

One possible explanation for the decrease of the lattice parameter at high doses could be the uptake of adventitious oxygen during the irradiation process. As mentioned above, the incorporation of oxygen into the crystaline structure of ZrC is accompanied by a contraction of the unit cell parameter. Zirconium carbide is well known for its high chemical sensititivity to oxygen impurities. Although the ion irradiations in this study were conducted in high vacuum conditions ($< 10^{-6}$ Pa), some residual oxygen and other hydrocarbon impurities are present in the irradiation chamber [55]. These impurities could oxidize target materials that are oxygen-sensitive during ion irradiation studies. ZrC has been reported to be subject to radiation-enhanced or radiation-induced oxidation at room temperature, even under vacuum (on the order of 10^{-6} Pa) [52]. Oxygen enrichment has also been observed in ZrC implanted with argon and xenon ions [56,57]. In the present work, the formation of ZrO_2 phases in the irradiated samples was supported by GIXRD measurements at low incident angles. Additionally, Electron Energy Loss Spectroscopy (EELS) analysis presented in a sister paper [58] revealed an enrichment of oxygen beneath the surface of both irradiated and unirradiated ZrC, corroborating similar observations from other authors. Based on these findings, it is possible that the diffusion of oxygen atoms may be enhaced during the high temperature irradiation of ZrC. The update of adventitious oxygen can explain the observed decrease in lattice parameter near the surface.

In the irradiated samples, radiation enhanced diffusion (RED) is assisted by a linear superposition of different possible diffusion paths, such as monovacancies, divacancies, and dislocation lines, among others. These diffusion pathways can facilitate the ingress of oxygen atoms into the implantation layer, producing an oxycarbide compound that is isostructural with ZrC. Gosset et al. [17] investigated the influence of oxygen content on the radiation response of ZrC. They found that ZrC and ZrO_xC_y compounds follow the same type of microstructural evolution under radiation conditions, with oxycarbides showing a delay in the saturation fluence with respect to carbides. At high doses, such as those used in this study, entangled dislocation networks and vacancies may favor the dissolution of oxygen into ZrC. However, the exact mechanism of oxygen uptake under irradiation conditions remains to be elucidated in future work.

3.2.2. *Raman spectroscopy*

Fig. 10 shows the Raman spectra of the control and irradiated samples. The spectra exhibit four predominant Raman bands centered around 200, 275, 515, and 600 cm^{-1}. These spectra are very similar to those obtained in single crystals of ZrC with sub-stoichiometric compositions [59,60]. The first-order Raman spectrum in ZrC_{1-x} has been attributed to the presence of carbon vacancies that destroy the local inversion symmetry of the ideal NaCl rock-salt structure, enabling defect-induced Raman scattering to be observed. The vacancy-induced first-order Raman spectrum resembles the phonon density of states (DOS) in ZrC. The low frequency Raman peaks (transverse acoustic $\sim$204 cm^{-1} and longitudinal $\sim$275 cm^{-1}) are produced by acoustic phonons, while the high frequency peaks (transverse optic $\sim$515 cm^{-1} and longitudinal optic $\sim$600 cm^{-1}) are due to optical phonons.

A comparison of the unirradiated and as-irradiated spectra shows that the Raman peaks associated with vacancy defects became more intense and broader when increasing the radiation dose. Similar radiation-induced changes have been previously observed in Raman studies of ion irradiated ZrC [60,61]. These variations of the peak properties have been ascribed to the increasing number of carbon vacancies generated by irradiation. Heavy ion irradiation of ZrC results in the formation of point defects that distort the local structure of the material causing the appearance of the defect-induced Raman scattering as described above. Previous *ab initio* calculations have shown that carbon-related defects (V_c and C_is) have lower defect formation

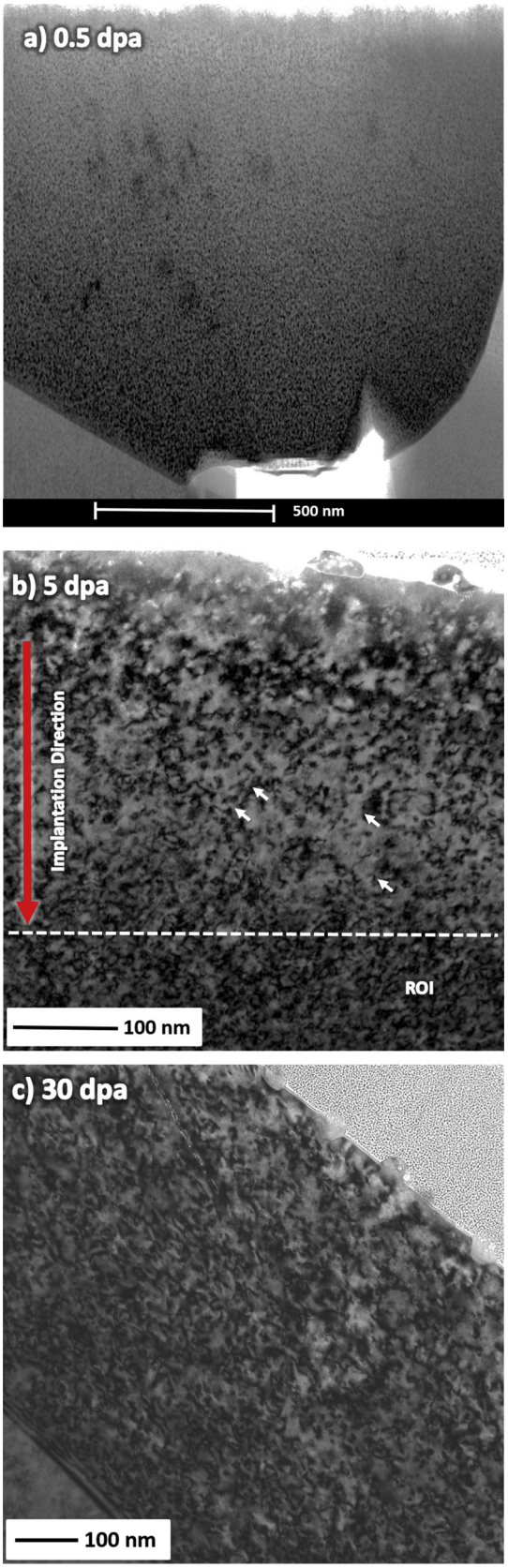

Fig. 9. (a) On-Zone STEM Bright Field Image of the specimen irradiated to 0.5 dpa showing black dot defects, (b) Brigth Field Image of the specimen irradiated to 5 dpa showing the tangle dislocation network. Some dislocation loops with double arc constrast are indicated by white arrows, (c) Bright Field Image of the specimen irradiated to 30 dpa showing the tangle dislocation network.

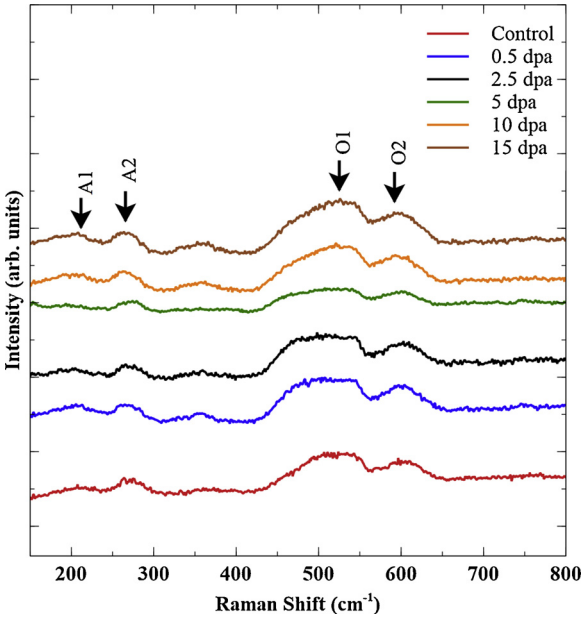

Fig. 10. Raman spectra for ZrC irradiated at various doses.

energy than other types of point defects in ZrC_x [22,62]. Consequently, extended non-stoichiometric regions with a high concentration of carbon vacancies are expected to occur under irradiation conditions. For this reason, it is not surprising that a direct correlation exists between the irradiation dose and the concentration of carbon vacancies, as indicated qualitatively by the changes in the Raman spectra for the irradiated samples. Besides these variations in vacancy-induced Raman bands, no new peaks are observed in the Raman spectrum of the irradiated samples. The similarity between the spectra for the irradiated and unirradiated specimens is indicative of the high microstructural stability of ZrC_x under irradiation conditions. This result is consistent with numerous computational and experimental studies which have shown the excellent radiation amorphization resistance of ZrC_x, [1,12,17,23,25,32,34,52].

4. Conclusion

The microstrutural evolution was examined for ZrC_x irradiated with 10 MeV Au^{3+} ions at 800 °C. No amorphization was observed in any of the irradiated samples, confirming the superior radiation stability of ZrC. Oxidation of the near surface area of the control and irradiated specimens was detected by GIXRD. Nanosized, discrete ZrO_2 nodules were observed to grow over the surface. BFTEM micrographs revealed that "black dot" defects were formed after irradiation to ~0.5 dpa. A further dose increase to 5 dpa produced coarsening of the microstructure and formation of tangled dislocation networks. Beyond this dose, little change was observed in the irradiated microstructure, which suggested that a balance had been reached between irradiation damage buildup and dynamic annealing of defects. The dose dependence of the lattice parameter, and microstrain, indicated that the defect structure changed at doses close to ~2.5 dpa. This change could be ascribed to the coalescence of dislocation loops to form tangled dislocation networks. Additionally, the evolution of the unit cell also showed that oxygen uptake could occur in samples irradiated to high doses. The oxygen uptake at high doses might be assisted by radiation-enhanced diffusion processes and by the changing microstructure (i.e. pipe diffusion at high doses). Finally, Raman spectroscopy analysis showed an increase in ZrC_x non-stochiometry after irradiaton. This is due to an increase in carbon vacancies produced by the irradiation.

The coupling of synergistic techniques used in this study provided a more comprehensive view of the irradiation response of ZrC_x ceramics

in the operational range of high temperature gas-cooled nuclear reactors. This work identified specific relationships between dose and microstructure after irradiation, revealing the mechanisms of damage production in ZrC_x, i.e., black-spot nucleation, as well as formation and evolution of dislocation loops. The results indicated that ZrC_x is a promising candidate for high temperature nuclear applications, although precautions must be taken to prevent its oxidation during reactor operation.

Declaration of Competing Interest

The authors of the paper of the manuscript "**The irradiation response of ZrC ceramics under 10 MeV Au^{3+} ion irradiation at 800 ºC**" have not conflict of interest to declare.

Acknowlegements

This research was supported by a Nuclear Regulatory Commission Faculty Development GrantNRC-HQ-84-15-G-0044 and by the Ceramics program of the U.S. National Science Foundation as part of project DMR 1742086. The microscopy work was conducted at the Electron Microscopy Center (EMC) of the University of Missouri Columbia with partial funding through the EMC Excellence Microscopy Award.

References

[1] H.F. Jackson, W.E. Lee, Properties and characteristics of ZrC, in: R.J.M. Konings (Ed.), Compr. Nucl. Mater. Elsevier, Oxford, 2012, pp. 339–372.
[2] M.M. Opeka, I.G. Talmy, E.J. Wuchina, J.A. Zaykoski, S.J. Causey, Mechanical, thermal, and oxidation properties of refractory Hafnium and Zirconium compounds, J. Eur. Ceram. Soc. 19 (1999) 2405–2414.
[3] T. Ogawa, K. Ikawa, Reaction of Pd with SiC and ZrC, High Temp. Sci. 22 (1986) 179–193.
[4] Y.-K. Yang, T.R. Allen, The measurement of silver diffusivity in zirconium carbide to study the release behavior of 110mAg in the ZrC TRISO-coated nuclear fuel particle, J. Nucl. Mater. 470 (2016) 76–83.
[5] Y. Katoh, G. Vasudevamurthy, T. Nozawa, L.L. Snead, Properties of zirconium carbide for nuclear fuel applications, J. Nucl. Mater. 441 (2013) 718–742.
[6] G. Vasudevamurthy, T.W. Knight, E. Roberts, T.M. Adams, Laboratory production of zirconium carbide compacts for use in inert matrix fuels, J. Nucl. Mater. 374 (2008) 241–247.
[7] G. Vasudevamurthy, T.W. Knight, T.M. Adams, E. Roberts, Production and characterization of ZrC-UC inert matrix composite fuel for gas fast reactors, Nucl. Technol. 173 (2011) 200–209.
[8] X.D. Yang, Z.M. Xie, S. Miao, R. Liu, W.B. Jiang, T. Zhang, X. Wang, Q. Fang, C. Liu, G. Luo, X. Liu, Tungsten-zirconium carbide-rhenium alloys with extraordinary thermal stability, Fusion Eng. Des. 106 (2016) 56–62.
[9] K. Minato, T. Ogawa, K. Sawa, A. Ishikawa, T. Tomita, S. Iida, H. Sekino, Irradiation experiment on ZrC-Coated fuel particles for high-temperature gas-cooled reactors, Nucl. Technol. 130 (2000) 272–281.
[10] K. Minato, T. Ogawa, Advanced concepts in triso fuel, in: R.J.M. Konings (Ed.), Compr. Nucl. Mater. Elsevier, Oxford, 2012, pp. 215–236.
[11] I.E. Porter, T.W. Knight, M.C. Dulude, E. Roberts, J. Hobbs, Design and fabrication of an advanced TRISO fuel with ZrC coating, Nucl. Eng. Des. 259 (2013) 180–186.
[12] L.L. Snead, Y. Katoh, S. Kondo, Effects of fast neutron irradiation on zirconium carbide, J. Nucl. Mater. 399 (2010) 200–207.
[13] G. Vasudevamurthy, Y. Katoh, J. Aihara, K. Sawa, L.L. Snead, Microstructure and mechanical properties of heat-treated and neutron irradiated TRISO-ZrC coatings, J. Nucl. Mater. 464 (2015) 245–255.
[14] D. Craciun, G. Socol, D. Simeone, S. Behdad, B. Boesl, B. Vasile, V. Craciun, Structural and mechanical properties changes induced in nanocrystalline ZrC thin films by Ar ion irradiation, J. Nucl. Mater. 468 (2016) 78–83.
[15] S. Gomès, L. David, J. Roger, G. Carlot, D. Fournier, C. Valot, M. Raynaud, Thermal conductivity degradation induced by heavy ion irradiation at room temperature in ceramic materials, Eur. Phys. J. Spec. Top. 153 (2008) 87–90.
[16] C. Jensen, M. Chirtoc, N. Horny, J.S. Antoniow, H. Pron, H. Ban, Thermal conductivity profile determination in proton-irradiated ZrC by spatial and frequency scanning thermal wave methods, J. Appl. Phys. 114 (2013) 133509.
[17] D. Gosset, M. Dollé, D. Simeone, G. Baldinozzi, L. Thomé, Structural behaviour of nearly stoichiometric ZrC under ion irradiation, Nucl. Instrum. Methods Phys. Res. Sect. B Beam Interact. with Mater. Atoms 266 (2008) 2801–2805.
[18] Y. Huang, B.R. Maier, T.R. Allen, Irradiation-induced effects of proton irradiation on zirconium carbides with different stoichiometries, Nucl. Eng. Des. 277 (2014) 55–63.
[19] S. Pellegrino, L. Thomé, A. Debelle, S. Miro, P. Trocellier, Damage production in carbide single crystals irradiated with MeV heavy ions, Nucl. Instruments Methods Phys. Res. Sect. B Beam Interact. with Mater. Atoms 307 (2013) 294–298.
[20] S. Agarwal, A. Bhattacharya, P. Trocellier, S.J. Zinkle, Helium induced microstructure damage, nano-scale grain formation and helium retention behaviour of ZrC, Acta Mater. 163 (2019) 14–27.
[21] B. Wei, Y. Wang, H. Zhang, D. Wang, S. Peng, Y. Zhou, Microstructure evolution of nonstoichiometric $ZrC_{0.6}$ with ordered carbon vacancies under ion irradiation, Mater. Lett. 228 (2018) 254–257.
[22] S. Kim, I. Szlufarska, D. Morgan, Ab initio study of point defect structures and energetics in ZrC, J. Appl. Phys. 107 (2019) 053521.
[23] M.-J. Zheng, I. Szlufarska, D. Morgan, Defect kinetics and resistance to amorphization in zirconium carbide, J. Nucl. Mater. 457 (2015) 343–351.
[24] M. Jiang, J.W. Zheng, H.Y. Xiao, Z.J. Liu, X.T. Zu, A comparative study of the mechanical and thermal properties of defective ZrC, TiC and SiC, Sci. Rep. 7 (2017) 9344.
[25] L. Van Brutzel, J.P. Crocombette, Classical molecular dynamics study of primary damage created by collision cascade in a ZrC matrix, Nucl. Instrum. Methods Phys. Res. Sect. B Beam Interact. Mater. Atoms 255 (2007) 141–145.
[26] G.S. Was, Challenges to the use of ion irradiation for emulating reactor irradiation, J. Mater. Res. 30 (2015) 1158–1182.
[27] G.S. Was, R.S. Averback, Radiation damage using ion beams, in: R.J.M. Konings (Ed.), Compr. Nucl. Mater. Elsevier, Oxford, 2012, pp. 195–221.
[28] G.S. Was, The radiation damage event, Fundamentals of Radiation Materials Science, Springer New York, New York, NY, 2017, pp. 3–76.
[29] J. Gan, Y. Yang, C. Dickson, T. Allen, Proton irradiation study of GFR candidate ceramics, J. Nucl. Mater. 389 (2009) 317–325.
[30] C.J. Ulmer, A.T. Motta, M.A. Kirk, In situ ion irradiation of zirconium carbide, J. Nucl. Mater. 466 (2015) 606–614.
[31] J. Gan, M. Meyer, R. Birtcher, T. Allen, Microstructure evolution in ZrC irradiated with Kr ions, J. ASTM Int. 3 (2006) 12376.
[32] S. Pellegrino, J.P. Crocombette, A. Debelle, T. Jourdan, P. Trocellier, L. Thomé, Multi-scale simulation of the experimental response of ion-irradiated zirconium carbide: role of interstitial clustering, Acta Mater. 102 (2016) 79–87.
[33] R.V. Sara, The system zirconium-carbon, J. Am. Ceram. Soc. 48 (1965) 243–247.
[34] S.J. Zinkle, J.T. Busby, Structural materials for fission & fusion energy, Mater. Today 12 (2009) 12–19.
[35] S.J. Zinkle, G.S. Was, Materials challenges in nuclear energy, Acta Mater. 61 (2013) 735–758.
[36] ASTM, ASTM C373-14 standard test method for water absorption, bulk density, apparent porosity, and apparent specific gravity of fired Whiteware products, Astm C373-88, (1999).
[37] Y. Zhang, M.L. Crespillo, H. Xue, K. Jin, C.H. Chen, C.L. Fontana, J.T. Graham, W.J. Weber, New ion beam materials laboratory for materials modification and irradiation effects research, Nucl. Instrum. Methods Phys. Res. Sect. B Beam Interact. Mater. Atoms 338 (2014) 19–30.
[38] M.L. Crespillo, J.T. Graham, Y. Zhang, W.J. Weber, In-situ luminescence monitoring of ion-induced damage evolution in SiO2 and Al2O3, J. Lumin. 172 (2016) 208–218.
[39] M.L. Crespillo, J.T. Graham, Y. Zhang, W.J. Weber, Temperature measurements during high flux ion beam irradiations, Rev. Sci. Instrum. 87 (2016) 024902.
[40] J.F. Ziegler, M.D. Ziegler, J.P. Biersack, SRIM - the stopping and range of ions in matter (2010), Nucl. Instrum. Methods Phys. Res. Sect. B Beam Interact. Mater. Atoms 268 (2010) 1818–1823.
[41] R.E. Stoller, M.B. Toloczko, G.S. Was, A.G. Certain, S. Dwaraknath, F.A. Garner, On the use of SRIM for computing radiation damage exposure, Nucl. Instrum. Methods Phys. Res. Sect. B Beam Interact. Mater. Atoms 310 (2013) 75–80.
[42] Y. Zhang, M.A. Tunes, M.L. Crespillo, F. Zhang, W.L. Boldman, P.D. Rack, L. Jiang, C. Xu, G. Greaves, S.E. Donnelly, L. Wang, W.J. Weber, Thermal stability and irradiation response of nanocrystalline CoCrCuFeNi high-entropy alloy, Nanotechnology 30 (2019) 294004.
[43] J. Rodriguez-Carvajal, Fullprof suite, LLB Sacley and LCSIM Rennes, (2006) France.
[44] W.A. Rachinger, A correction for the α_1 α_2 doublet in the measurement of widths of x-ray diffraction lines, J. Sci. Instrum. 25 (1948) 254–255.
[45] B. Wei, L. Chen, Y. Wang, H. Zhang, S. Peng, J. Ouyang, D. Wang, Y. Zhou, Densification, mechanical and thermal properties of ZrC_{1-x} ceramics fabricated by two-step reactive hot pressing of ZrC and ZrH2 powders, J. Eur. Ceram. Soc. 38 (2018).
[46] S.E. Landwehr, G.E. Hilmas, W.G. Fahrenholtz, I.G. Talmy, S.G. DiPietro, Microstructure and mechanical characterization of ZrC–Mo cermets produced by hot isostatic pressing, Mater. Sci. Eng. A 497 (December 1–2) (2008) 79–86.
[47] A.R. Stokes, A.J.C. Wilson, The diffraction of x rays by distorted crystal aggregates - I, Proc. Phys. Soc. 56 (1944) 174–181.
[48] F. Réjasse, O. Rapaud, G. Trolliard, O. Masson, A. Maître, Experimental investigation and thermodynamic evaluation of the C–Hf–O ternary system, J. Am. Ceram. Soc. 100 (2017) 3757–3770.
[49] P. Barnier, F. Thévenot, Synthesis and hot-pressing of single-phase ZrC_xO_y and two-phase ZrC_xO_y/ZrO_2 materials, Int. J. High Technol. Ceram. 2 (Janauary 4) (1986) 291–307.
[50] M. Gendre, A. Maître, G. Trolliard, Synthesis of zirconium oxycarbide (ZrCxOy) powders: influence of stoichiometry on densification kinetics during spark plasma sintering and on mechanical properties, J. Eur. Ceram. Soc. 31 (2011) 2377–2385.
[51] B.C. Larson, X-ray diffuse scattering near Bragg reflections for the study of clustered defects in crystalline materials, Diffuse Scattering and the Fundamental Properties of Materials, Momemtum Press, New York, 2009, pp. 139–160.
[52] D. Gosset, M. Dollé, D. Simeone, G. Baldinozzi, L. Thomé, Structural evolution of zirconium carbide under ion irradiation, J. Nucl. Mater. 373 (2008) 123–129.
[53] A. Debelle, J.P. Crocombette, A. Boulle, A. Chartier, T. Jourdan, S. Pellegrino, D. Bachiller-Perea, D. Carpentier, J. Channagiri, T. Nguyen, F. Garrido, L. Thomé, Lattice strain in irradiated materials unveils a prevalent defect evolution

mechanism, Phys. Rev. B Condens. Matter Mater. Phys. 2 (2018) 013604.
[54] S. Moll, Y. Zhang, L. Debelle, J.P. Thomé, Z. Crocombette, J. Zihua, Jagielski, W.J. Weber, Damage processes in MgO irradiated with medium-energy heavy ions, Acta Mater. 88 (2015) 314–322.
[55] J. Wang, M.B. Toloczko, K. Kruska, D.K. Schreiber, D.J. Edwards, Z. Zhu, J. Zhang, Carbon Contamination During Ion Irradiation - Accurate Detection and Characterization of its Effect on Microstructure of Ferritic/Martensitic Steels, Sci. Rep. 7 (2017) 15813.
[56] G. Gutierrez, N. Toulhoat, N. Moncoffre, Y. Pipon, N. Djourelov, A. Maître, M. Gendre, P. Nedelec, High temperature annealing of Xe implanted ZrC0.95O0.05 investigated by RBS, TEM and PAS-DBS, Prog. Nucl. Energy. 57 (2012) 57–61.
[57] C. Martin, K.H. Miller, H. Makino, D. Craciun, D. Simeone, V. Craciun, Optical properties of Ar ions irradiated nanocrystalline ZrC and ZrN thin films, J. Nucl. Mater. 488 (2018) 16–21.
[58] R. Florez, Microstructural Evolution of Zirconium Carbide (ZrC_x) Ceramics under Irradiation Conditions, Doctoral Dissertations. 2821 (2019), pp. 60–101 https://scholarsmine.mst.edu/doctoral_dissertations/2821.
[59] H. Wipf, M.V. Klein, W.S. Williams, Vacancy-Induced and Two-Phonon Raman Scattering in ZrC_x, NbC_x, HfC_x, and TaC_x, Phys. Status Solidi 108 (1981) 489–500.
[60] S. Pellegrino, L. Thomé, A. Debelle, S. Miro, P. Trocellier, Radiation effects in carbides: TiC and ZrC versus SiC, Nucl. Instrum. Methods Phys. Res. Sect. B Beam Interact. Mater. Atoms 327 (2014) 103–107.
[61] W. Bao, J. Liu, X. Wang, H. Zhang, J. Xue, S. Sun, F. Xu, J. Xue, G. Zhang, Structural evolution in ZrC-SiC composite irradiated by 4 MeV Au ions, Nucl. Instrum. Methods Phys. Res. Sect. B Beam Interact. Mater. Atoms 434 (2018) 23–28.
[62] Y. Zhang, J. Wang, B. Liu, J. Wang, H. Zhang, Understanding the Behavior of Native Point Defects in ZrC by First-Principles Calculations, J. Am. Ceram. Soc. 97 (2014) 4024–4030.